Published in final edited form as:
J Magn Reson Imaging. 2013 February ; 37(2): 282–293. doi:10.1002/jmri.23717.

Functional MRI of the kidneys

Jeff L. Zhang, Ph.D.[1], **Henry Rusinek, Ph.D.**[2], **Hersh Chandarana, M.D.**[2], and **Vivian S. Lee, M.D., Ph.D.**[1]

[1]Department of Radiology, University of Utah School of Medicine, Salt Lake City, UT

[2]Department of Radiology, New York University School of Medicine, New York, NY

Abstract

Renal function is characterized by different physiologic aspects, including perfusion, glomerular filtration, interstitial diffusion and tissue oxygenation. MRI shows great promise in assessing these renal tissue characteristics noninvasively. The last decade has witnessed a dramatic progress in MRI techniques for renal function assessment. This article briefly describes relevant renal anatomy and physiology, reviews the applications of functional MRI techniques for the diagnosis of renal diseases, and lists unresolved issues that will require future work.

Keywords

kidney; magnetic resonance imaging; functional

INTRODUCTION

The accurate assessment of kidney function is important in both the clinic and research. Impairment in renal function precedes anatomic changes such as atrophy, and early detection of functional loss allows more options for treatment and potentially a delay or halt in disease progression. Functional assessment is also important in renal transplantation, the only effective therapeutic option after renal failure. Within the first two years, about a third of grafted kidneys manifest an episode of graft dysfunction due to various causes. Reliable functional monitoring for grafted kidney is desirable for both short-term and long-term management. The most commonly used measure of renal function is serum creatinine. However, serum creatinine has well known limitations, particularly insensitivity to early renal dysfunction, especially in chronic disease. Elevated serum creatinine is often discovered only in the late stages of disease, when substantial and sometimes irreversible renal damage takes place.

In the past decade, magnetic resonance imaging (MRI), conventionally used for tissue anatomic imaging, has been explored as an important and versatile tool for assessing the function of the kidneys. Techniques, such as dynamic contrast enhanced (DCE) MRI, diffusion-weighted MRI (DWI), blood oxygenation level dependent (BOLD) MRI and arterial spin labeling (ASL), enable noninvasive evaluation of various aspects of renal function ranging from perfusion to filtration to oxygenation. These techniques show promise in replacing the invasive techniques, e.g. oxygen micro-probe for oxygenation, which are currently limited to animal experiments.

Address Correspondence to: Jeff L. Zhang, Department of Radiology, University of Utah, 729 Arapeen Drive, Salt Lake City, UT 84108; Lei.Zhang@hsc.utah.edu Tel: 801 581 8410.

In recent years, several reviews on the role of MRI in evaluating renal function have been published (1-6). This review article covers the recent progress in the area of functional MRI of the kidney. We begin with a short introduction of renal anatomy and physiology, followed by the overview of various MRI techniques (DCE, DWI, BOLD, ASL) that can assess renal function. We briefly discuss application of these techniques in evaluation of renal diseases and major directions for further development of renal functional MRI.

RENAL ANATOMY AND PHYSIOLOGY

Overall structure

The kidney consists of predominantly a peripheral **cortex** and more centrally, the renal **medulla**, which is configured as multiple internally situated cone-shaped tissues called **pyramids** (Figure 1a). The tips of each pyramid converge near the center of the kidney into the area known as a **calyx**. Urine collects in the **renal pelvis** and then flows through the ureter into the bladder. The space where renal pelvis resides, termed as renal **hilum**, contains the distal end of **renal artery** and the origin of **renal vein**. Each of the two (left and right) renal arteries receives ~10% of cardiac output. Within the kidney, blood perfusion in cortex is ~400-500 ml/min/100g, while medulla is less perfused, ~100-150 ml/min/100g, as measured by computed tomography technique (7,8).

Nephron

A typical kidney contains about 1 million nephrons. Each nephron consists of a filtering component, called renal corpuscle, and a tubule where reabsorption and secretion take place (Figure 1b). The **renal corpuscle**, a ball-shaped structure, consists of its exterior component called a **Bowman's capsule** that holds a compact bundle of capillary loops called a **glomerulus**. Blood in afferent arteriole enters glomerulus, gets filtered there, and exits through an efferent arteriole. Filtration results in about 20% of the incoming renal plasma passing through the glomerular membrane; first into Bowman's capsule, then into the proximal tubule. This fluid is accompanied by solutes with molecular weight < 6000 Dalton. Glomerular filtration rate (GFR, ml/min) is normally around 60 ml/min, or a total of ~120 ml/min for both kidneys. Urine flow is only ~1 ml/min. This huge discrepancy is due to the reabsorption of glomerular filtrate back into the blood.

Tubule and peri-tubular capillaries

The renal tubule extends from Bowman's capsule, and consists of: **proximal tubule (PT)**, **loop of Henle (LH)**, and **distal tubule (DT)**. The PT and DT are mostly in renal cortex, and LH, connecting PT and DT, is deep in the renal medulla (Figure 1b). DT joins a collecting duct which ultimately terminates in a calyx. In the renal cortex, peri-tubular capillaries are distributed around the PT and DT. Some efferent arterioles extend down to medulla, giving rise to **descending vasa recta (DVR)** (Figure 1b). Reabsorbed water and solutes from the tubules rejoins the circulation via the capillaries and vasa recta.

Water and sodium reabsorption

In the proximal tubule, a large fraction (~65%) of sodium is reabsorbed back via Na-H antiporter. Due to osmotic force, water is reabsorbed across highly permeable PT. The descending thin limb of LH is not permeable to sodium, but ~10% of water is reabsorbed there. In the thick ascending limb, active transcellular reabsorption by Na-K-2Cl symporter becomes a dominant factor, leading to ~25% of filtered sodium. In DT, about 5% of sodium is reabsorbed by Na-Cl symporter. The transporters for active transcellular sodium reabsorption are driven by Na-K-ATPase, or sodium pumps. The main function of the Na-KATPase is to pump sodium from epithelium into interstitium, at the expense of ATP. Note that in renal medulla where perfusion is low, the active transport of sodium results in low tissue oxygenation or hypoxia state (10-20 mmHg, compared with 50-60 mmHg in cortex) (9,10). Water does not permeate the ascending limbs and the distal tubule. In the collecting ducts, water reabsorption is controlled by antidiuretic hormone (ADH or vasopressin) secreted from the pituitary gland. The bulk flow of salt and water from interstitium to peritubular capillary results from hydrostatic and oncotic forces, also called Starling forces.

Renal autoregulation

Due to the myogenic mechanism and renin-angiotensin system, renal blood flow (RBF) and GFR are relatively stable in spite of variable blood pressure in renal artery. Decreased arterial pressure leads to reduced tubular Na concentration, which is sensed by specialized cells - macula densa. Resulting stimulation of renin secretion preferentially constricts efferent arterioles and leads to preserved GFR. Angiotensin-converting enzyme (ACE) inhibitors inhibit the effect of renin, and are useful in detecting renovascular hypertension.

Diuretics

A diuretic is any drug that elevates the rate of urine production. Different types of diuretics act on different tubular segments. Water loading is widely used in MRI research to suppress secretion of ADH and reduce water reabsorption along the collecting ducts. Furosemide, on other hand, blocks sodium reabsorption in the thick ascending limb of loop of Henle, thus reducing ATP consumption and counteracting medullary hypoxia.

FUNCTIONAL MRI TOOLS

Since the function of the kidney centers on the fluid regulation, MRI is naturally suited for in-vivo measurement of various aspects of renal function, such as perfusion, filtration, diffusion and oxygenation (Table 1).

Dynamic contrast enhanced (DCE) MRI

Before the advent of DCE MRI, dynamic renal scintigraphy using radioactive technetium-99m based tracers has been widely used for measuring renal function. DCE MRI for the kidney, also termed MR renography (MRR), has advantages over scintigraphy including no radiation exposure, inherently three-dimensional acquisition, and superior spatial resolution. Unlike scintigraphy, MRI can easily resolve the renal cortex from the medulla and collecting system. Through more realistic modeling DCE-MRI offers the potential to reveal in vivo renal properties that in the past could only be examined with biopsies, opening new windows into renal pathophysiology and clinical diagnosis.

Tracer kinetics and modeling—One key aspect of DCE-MRI analysis is the choice of model used to describe the transit of contrast in renal tissue. As reviewed recently (11), at this time there is no consensus about the best model for MRR.

A two-compartmental model, restricted to vascular and tubular compartments, has been introduced by several groups. The major attraction of such model, especially its graphical Patlak-plot “upslope” implementation (12), is its simplicity. However, these two-compartmental models ignore the transit of the tracer out of the tubular compartment and strongly depend on the arbitrary time interval over which a slope is calculated. Annet et al (13) refined the two-compartment model by introducing the delay and dispersion of the bolus between the aorta and renal vasculature and accounting for the efflux from the tubular compartment as an exponential decay. Sourbron et al (14) extended this model for measuring both renal perfusion and GFR. A comparison study by Buckley et al (15) found that the refined model fitted experimental data better but it overestimated GFR. Koh et al

(16) validated a more elaborate parallel two-pathway model, vascular (from renal artery to vein) and tubular (from renal artery to tubules).

More elaborate modeling is predicated on our ability to measure contrast in two subregions of the kidney, cortex and medulla (17). Such three-compartment models were developed by Lee and Zhang et al (18,19). Three compartmental models have the potential of providing functional information about tubules. The papers by Buckley et al (15) and Bokacheva et al (11) compared some of the models, and provide some recommendations for their use.

In addition to the kinetic modeling of DCE data, there are other considerations worth noting, including the effects of errors in arterial input function estimates and efforts to convert MR signal intensity into gadolinium concentrations for modeling, each of which are discussed briefly below.

Estimating arterial input function (AIF)—Kinetic analysis of DCE data requires the knowledge of AIF. MR signals from arteries are susceptible to several MR artifacts, including inflow effect, dephasing, partial-volume effect and flow pulsation. Figure 2 demonstrates the impact of inflow artifact. Mendichovszky and Cutajar et al (20,21) found that AIF strongly depends on the size of aortic ROI. Generally, two solutions have been proposed. Bauman and Rudin (22) used cortical signal as surrogate for arterial input and medullary signal as tissue retention function. Zhang et al (23) proposed a similar method but used the cortex-medulla difference as the tissue retention function for GFR estimation. This latter method utilized the fact that vascular and tubular pathways are coupled with each other and the subtraction of cortical and medullary signals gives roughly tracer retention in the collecting ducts. One drawback of these surrogate methods is that they do not provide information on renal blood flow.

Other studies have proposed to improve the measured AIF. Parker et al (24) and Wang et al (25) averaged AIFs obtained from a group of controls and applied this population-averaged AIF to the analysis of new patients. Since AIF partially depends on the cardiac output (CO) of the patient, this method assumes a relatively homogeneous population. Roberts et al (26) proposed a double-bolus technique to compensate mis-sampling of the first pass of AIF at low temporal resolution and showed that the method improved the precision of parameters. Zhang et al (27) developed a method for constraining AIF using CO of the patient, based on indicator dilution theory, which relates the injected dose, CO, and the area under the first pass of AIF. Using phase-contrast MRI, CO can be conveniently measured in <1 minute in the same imaging session as DCE MRI.

Quantification of tracer concentration—Quantitative analysis of MRR data typically requires image data to be converted to concentration of tracer in the tissue of interest. For widely used T_1-wieghted MRR, tracer concentration is related to tissue $1/T_1{}^0$ by the following linear relationship,

$$C^{Gd}=\left(\frac{1}{T_1}-\frac{1}{T_1^0}\right)\frac{1}{r_1} \quad (1)$$

where C^{Gd} is the time-varying concentration of contrast medium, T_1 is the time varying longitudinal relaxation, $T_1{}^0$ is the spin-lattice relaxation time in absence of contrast medium, and r_1 is the T_1 relaxivity of the contrast medium. T_1 values can be derived from the acquired signals and the appropriate sequence-specific formula (28).

An estimate of tracer concentration from Eq. [1] requires knowledge of r_1 and $T_1{}^0$ in renal tissue and blood. For Gd-DTPA at 1.5T, Shuter et al (29) measured r_1 to be 1.2 $s^{-1}mM^{-1}$ for cortex and 1.3-1.6 $s^{-1}mM^{-1}$ for medulla. Morkenborg et al (30) measured cortical r_1 to be 1.1 s-$^{1}mM^{-1}$. These reduced values compared with plasma r (4-5 $s^{-1}mM^{-1}$ 1 (30)) may be attributed to compartmentalization between reabsorbed water and tubular water, as analyzed by Donahue et al (31). T_1^0 can be measured by several rapid methods, such as variable flip angle method (32) and inversion recovery method (33,34).

Limitations and future needs of DCE-MRI 1—

1. Quantification of tracer concentration in renal tissue relies on the determination of kidney in vivo T_1 values and on relaxivity of gadolinium, which may differ from in vitro estimates.
2. Over the time course of 3 – 5 min, when gadolinium contrast transits through the kidneys, there may be significant movement artifact in the MRI data. Manual correction of such movement artifact can be avoided by automatic registration techniques (35,36). The use of coronal imaging and the consequent restriction of movement to being mostly in-plane reduce the complexity of coregistration software.
3. Tracer kinetic analysis of DCE MRI data requires accurate segmentation of the kidneys and, for applying some complex models, separation of renal cortex and medulla (17,37,38). Mis-segmentation could cause partial volume effect that lowers the accuracy of GFR estimates (39).
4. Tracer kinetic models to interpret gadolinium concentration curves often depend on accurate measures of the arterial input function. Coronal acquisition helps minimize AIF inflow artifact. Moreover, some regularization of the AIF might give improvements (27).
5. Some Gd-based contrast agents may cause nephrogenic systemic fibrosis (NSF) in patients with diminished renal function (40,41). Non-contrast MRI techniques as we will discuss have been intensively explored in recent years.

Applications—With the capability of measuring single-kidney GFR, MR renography has the potential of diagnosing several renal diseases.

1. Renovascular hypertension (RVH): RVH as one type of correctable hypertension is caused by renal artery stenosis (RAS). Arterial narrowing could be due to atherosclerosis or fibromuscular dysplasia. Because patients can have idiopathic hypertension, it is important to identify correctly patients who have clinically significant RAS and who will benefit from revascularization surgery. Captopril renography using nuclear medicine techniques have been widely used in the past. This method can also be adapted to MRI where GFR measurementsbefore and after angiotensin-converting enzyme (ACE) inhibitor are compared to determine whether the RAS has activated a renin-mediated hypertension (42). In 1996, Grenier et al (43) first demonstrated the feasibility of ACE-inhibitor renography using MRI. Recently, Lee et al (44,45) improved the protocol by using low-dose contrast medium and shortening the procedure into <0.5hr, and analyzed the data with newly developed tracer kinetic modeling techniques.
2. Functional urinary obstruction: Urinary obstruction often causes hydronephrosis (a dilation of renal pelvis calyces) and eventually leads to renal failure. Renal function loss due to urinary obstruction can be assessed by measuring ‘differential renal function (DRF)’ from dynamic MR urography (46). Methods for calculating DRF are based on either the parenchyma volume (47), the area under tubular phase of signal vs. time curve (48), or Rutland-Patlak plot (49). In addition, renal transit

time (RTT), defined as the time between tracer appearance in the kidney and in ureter (50), was shown to be useful in differentiating between normal and obstructive kidneys. The combination of high-resolution morphologic imaging, DRF and RTT, from a single MRI session, provides a comprehensive tool for diagnosing urinary obstruction.

3. Renal transplant: Complications in the early post-transplantation period (~1-2 weeks) could lead to delayed graft function and impact the long-term outcome of renal grafts. The major complication is acute tubular necrosis (ATN), which is essentially an ischemic injury to the tubules. ATN is characterized by reduced blood flow, reduction in GFR and tubular dysfunction. Figure 3 compares perfusion maps of a healthy kidney and an ischemic transplant. Other causes include acute rejection (AR) of different types, arteriole or venous thrombosis, nephrotoxicity and ureteric obstruction.

In 1997, Szolar et al (51) aimed to differentiate ATN, AR, normal graft cases using a semi-quantitative analysis of MR enhancement curves and found that, compared to normal cases, AR cases displayed lower cortical and medullary enhancement curves, while ATN cases showed distinct medullary enhancement curves. Agildere (52) demonstrated the potential of DCE MRI in differentiating AR and cyclosporine nephrotoxicity. Wentland et al (53) estimated cortical and medullary perfusion for renal transplants, and found that cortical and medullary perfusion of AR was significantly lower than that of normal and ATN cases. Their results were in agreement with Szolar et al (51). However, perfusion information alone could not differentiate ATN and normal cases. Realizing that ATN might affect tubular transit, Yamamoto et al (54) estimated mean transit times (MTT) using a three-compartment model and found a higher ratio of tubular MTT over whole-parenchyma MTT than successful transplant.

Diffusion-weighted MRI

Diffusion-weighted MRI (DWI) is designed to probe random microscopic motion, or diffusion, of water in tissue, and does not require exogenous contrast agent. The diffusion sequence incorporates a bipolar gradient into a spin echo sequence (Figure 4).

The dependence of measured signal S on the b values is given as:

$$S(b) = S(0) \cdot e^{-b \cdot ADC} \quad (2)$$

where ADC is apparent diffusion coefficient. ADC is one of the simplest parameters that reflect tissue microstructure. The estimation of ADC can be done by fitting signals acquired at different b values by Eq. [2]. In a detailed review, Kim et al (55) suggested a standardized sequence: breath-hold or respiratory triggered (using a navigator echo), single-shot echo-planar imaging, tri-directional gradients using b-values: 0, 400, and 800 sec/mm^2.

Applications of ADC in renal fibrosis and dysfunction—Normal renal function involves multiple processes of water transport, while worsening renal function (reduction in GFR) should lead to a decrease in water reabsorption, i.e. a lower rate of water transfer across interstitial space. This would potentially reduce diffusion. In addition, fibrosis formed in the process of chronic renal dysfunction may also restrict water diffusion. Several researchers have shown a positive correlation (R=~0.8) between ADC and GFR, estimated either with serum creatinine level (56,57) or renal scintigraphy (58,59). Recently Togao et al (60) studied the relationship between renal fibrosis and ADC in an animal model of unilateral ureteral obstruction (ureteral obstruction induces fibrosis in ~1 week), and found that the ADC of the obstructed kidneys decreased to 0.7×10^{-3} mm^2/sec on day three, and to

0.57×10^{-3} mm^2/sec on day seven (Figure 5). ADC of contralateral kidney remained stable at 0.9-1.0$\times10^{-3}$ mm^2/sec. As speculated by the authors and Thoeny et al (61), the decrease in ADC could be due to the increase in cell density in interstitial space.

Intra-voxel incoherent motion (IVIM) effect—IVIM extends the mono-exponential model from Eq. [2] by including microscopic motion attributable to microcirculation of blood (62,63),

$$S\ (b) = S\ (0) \cdot \left[F_p \cdot e^{-b \cdot D_p} + \left(1 - F_p\right) \cdot e^{-b \cdot D_r} \right], \quad (3)$$

where F_P is fast-component fraction, D_T is tissue diffusion coefficient, and D_P is pseudo-diffusion coefficient due to IVIM effect. With high capillary density and high blood flow, the kidney is expected to show a strong IVIM effect. Zhang et al (64) found that ADC values from mono-exponential fitting depend heavily on the b values used (Figure 6), and concluded that that mono-exponential model is not adequate for renal DWI data. The advantage of bi-exponential model in fitting renal DWI data was confirmed by Wittsack et al (65) who compared mono-exponential, bi-exponential and a distribution function model.

Limitations and future needs of IVIM—While mounting evidences suggest that the IVIM parameters may provide a non-invasive biomarker for renal perfusion, more work is needed.

1. DWI data of high quality is needed to improve the estimation precision of IVIM parameters, since error propagation from signal to F_P and D_P is much higher than that to ADC (66). Respiratory motion is a major problem that degrades DWI image quality.
2. The relative contributions of blood flow (perfusion) and tubular flow to the IVIM parameters are unclear. Quantitative measurement of perfusion based on DWI would require the separation of these different flow components that may contribute to the fast diffusion-decay component.

Blood oxygen level dependent (BOLD)

Although the kidney receives a high fraction of cardiac output (~10%), the renal medulla especially the inner medulla works in a state of hypoxia (O_2 partial pressure pO_2 ~10-20 mmHg). The hypoxic state of medulla is caused by 1) low oxygen delivery due to low vascular density in medulla and arterial-venous shunting, and 2) high oxygen consumption for active transcellular transport of sodium and chloride. Since renal tissue oxygenation is an important marker of renal dysfunction, there is considerable interest in noninvasive techniques to estimate intrarenal oxygenation. One possible approach is based on BOLD MRI. The presence of deoxyhemoglobin generates a susceptibility difference that locally perturbs the magnetic field and increases the spin-spin relaxation rate R_2^* of surrounding water (67). High R_2^* estimate corresponds to low tissue oxygenation. R_2^* is usually derived from multi-echo gradient recalled echo (mGRE) sequence (68).

Diuretic-enhanced BOLD—The frequently used diuretic in BOLD kidney experiments is *furosemide*, which acts by inhibiting Na-K-2Cl symporter in TAL of loop of Henle, thereby decreasing the activity of sodium pumps, and thus decreasing oxygen consumption. In 1996, Prasad et al (69) showed that both furosemide and water loading induced a decrease in medullary R_2^* (increase in pO_2). A time-resolved approach (70) was then implemented to record the temporal response of medullary R_2^* after water loading. Reasonable reproducibility of R_2^* measurement (3%-12%) has been evaluated by multiple studies (71-73).

Limitations and future needs of BOLD—First, high field strength such as 3T induces strong BOLD contrast, but may also cause severe bulk susceptibility artifact, e.g. due to the presence of bowel gas. Second, BOLD effect (or R_2*) relates to tissue oxygenation, but also depends on other variables, such as perfusion, vascular volume fraction and intrinsic spin-spin relaxation R_2. Better quantification of renal tissue oxygenation from BOLD data requires separating these other effects out.

Applications

1. Renal artery stenosis (RAS): There is increasing evidence that BOLD is sensitive to subtle intrarenal change induced by RAS, enabling the prediction of possible renal failure at an earlier stage. Juillard et al (74) observed increased R_2* in a pig model during progressive constriction of renal artery, indicating the important role of renal blood flow in maintaining renal tissue oxygenation. With the decrease in renal blood flow, oxygen content was consistently lower in the cortex than in the medulla, while in the contralateral kidney without artery constriction, oxygen content was slightly lower in medulla. This suggests that in progressive RAS, blood flow is better preserved in the medulla than in the cortex.

Textor et al (75) compared cortical and medullary R_2* values and their change after furosemide in human kidneys without RAS, with RAS but preserved kidney volume (‘viable’), and with total artery occlusion and renal atrophy (‘nonviable’). Normal kidneys experienced a rapid fall in R_2* values after furosemide, similar to Prasad’s study, due to the inhibition of Na reabsorption in TAL. The kidneys with RAS but preserved function had elevated R_2* (lower oxygenation) values at baseline, which dropped after furosemide. The atrophic kidneys with total arterial occlusion had reduced R_2* values and minimal change after furosemide, which was similar to renal allografts with acute dysfunction.

2. Renal transplant: The noninvasiveness feature of BOLD and its sensitivity to multiple physiologic factors make it suitable for the assessment of renal transplants. Current applications focus on the differentiation between acute rejection (AR) and acute tubular necrosis (ATN) as the cause for delayed graft function. Sadowski et al (76) showed that the medullary R_2* of AR cases was lower than that of normal or ATN cases, and cortical R_2* of ATN cases was higher than that of normal or AR cases. Djamali et al (77) obtained similar results, except that a significant reduction in medullary R_2* was detected in ATN, compared with normal cases. Compared to normal kidney, the ratio (M/C) of medullary R_2* to cortical R_2* was reduced in ATN and lowest in AR. The decreased M/C in ATN and AR are probably due to decreased oxygen consumption in delayed graft function. However, Han et al (78) observed abnormally higher medullary R_2* and M/C in ATN. This discrepancy was attributed to the shorter surgery to scan time (~10 days in Han et al compared with 29 days in Djamali et al). In the early stage of ATN, acute ischemia compromises oxygen delivery while oxygen consumption by the reabsorption is maintained. This results in a temporary decrease of oxygen bioavailability.

3. Diabetes: Diabetic patients are at high risk for developing chronic kidney disease. Renal damage occurs in multiple stages (79). Stage 1: at the onset of diabetes, there is an increase in the size and in glomerular filtration (hypertrophy and hyperfiltration); Stage 2: at 2-5 years after onset, if blood sugar level remains high, damage to glomerulus and thickening of the basal membrane occurs; Stage 3: at 5-15 years, if blood sugar level remains high, albumin appears in urine, and GFR and RBF decrease; Stage 4: urine albumin exceeds 200mg/L, indicating a serious damage to glomerulus. Accumulation of albumin and other protein blocks blood flow to capillaries, leading to end stage renal failure.

Epstein et al (80) compared mild diabetic patients (presumably stage 1 diabetes) and normal subjects of similar age with BOLD MRI. During water diuresis, medullary R_2* decreased in the normal subjects, but remained unchanged in the diabetic patients. Since a decrease in R_2* represents an increase in tissue oxygenation, this result presumably reflects a deficiency in medullary vasodilatation in diabetic subjects. Inducing diabetes in rats, dos Santos et al (81) detected a progressive decrease in pO_2 of both the cortex and medulla from day 0 to day 28 after the induction of diabetes, suggesting increased activity of sodium pumps. Similar result was found by Ries et al (82) (Figure 7). These studies support the use of BOLD to monitor changes in renal hemodynamics in diabetic patients at an early stage.

4. Other applications: BOLD imaging has the potential for a broad range of other clinical indications. With unilateral ureteral obstruction (UUO), an animal study with pigs after 24-hour UUO has shown increased cortical R_2* (i.e. lower oxygenation) and decreased medullary R_2* (i.e. higher oxygenation) (83). In human subjects with UUO (with duration 5-47 hours), Thoeny et al (84) observed decreased medullary R_2* and decreased cortical R_2*. The different change in cortical R_2* between the two studies could be due to the race difference, or the different durations of UUO. In patients with acute renal failure, Xiao et al (85) observed decreased cortical R_2* and even more decreased medullary R_2*, indicating increased oxygenation level in both cortex and medulla.

Arterial spin labeling (ASL) – non-contrast perfusion imaging

Originally developed for measuring cerebral perfusion (86,87), ASL uses magnetically labeled protons in arteries as endogenous tracer and is therefore completely non-invasive. Renal ASL has been validated by several studies, most of which used FAIR (flow sensitive alternating inversion recovery) for perfusion preparation and True-FISP (true fast imaging with steady precession) for data acquisition. Because SNR is low in ASL, multiple repetitions and high field (3T) are needed. ASL signal decays with blood T_1, so acquisitions must be performed within 1-2 sec of arterial labeling. Because acquisitions typically require labeled and unlabeled measurements and their subtraction, motion artifacts can impede accurate measurements. Song et al (88) demonstrated high-quality ASL images with free breathing by incorporating dual-navigator technique into FAIR and correcting mismatch between labeling slice and image slice (Figure 8). Most of the studies use a one compartment ASL model. Kiefer et al. (89) recently reported on a two-compartment model that accounts for delayed exchange between vascular and extra-vascular spaces. Such models require higher SNR and acquisition of multiple inversion time points.

In agreement with more established invasive techniques, ASL MR studies have estimated renal perfusion at ~300 ml/min/100g for cortex and ~100 ml/min/100g for medulla of healthy kidneys. Artz et al (90) showed good correlation between ASL measured perfusion and fluorescent microsphere method in a swine model. However, ASL values were consistently lower than microsphere estimates. More research is needed to validate ASL against reference technique in human subjects.

Other MRI techniques

We have focused on some of the main areas of functional renal MRI studies. Many other approaches are also in the exploratory phase including diffusion tensor imaging (DTI) to study the directionality of water diffusion (91-93), Na MRI to study corticomedullary sodium gradient (94-96) and MR elastography to evaluate tissue mechanical property (97,98).

FUTURE DIRECTIONS

MRI tools appear promising in estimating physiologic parameters for the diagnosis and monitoring of renal diseases. To achieve the promise, future studies are needed to resolve the following issues.

1. Given the challenges of respiratory and bulk motion, adjacent bowel gas, and spatial resolution demands, technical improvements in image quality are critical to advances in functional renal MRI.
2. Validation of quantitative models is critical for relating measured MRI data with specific and meaningful physiologic parameters. Examples include (1) the interpretation of BOLD measurements for oxygenation and perfusion, and (2) the differentiation of perfusion, filtration, and resorption changes on DWI and IVIM measurements.
3. With the broad array of tools available in renal MRI, we must combine multiple (especially non-contrast) MRI protocols in a same scan. Clinical studies are needed to refine multimodality applications.
4. Robust image registration and segmentation. Image registration to correct for motion artifacts and the segmentation of renal cortex and medulla have been major issues in the analysis of renal images. Readily available tools for co-registration of images from different MR sequences are also needed.

The trajectory of functional renal imaging over the past decade and the growth in interest in the field promise a bright future ahead. Without question, research advances in this field will benefit substantial patient populations with high impact.

Acknowledgments

Grant Support: NIH grants R01DK063183 and R01DK088375

REFERENCE

1. Prasad PV. Functional MRI of the kidney: tools for translational studies of pathophysiology of renal disease. American journal of physiology. 2006; 290(5):F958–974. [PubMed: 16601297]
2. Chandarana H, Lee VS. Renal functional MRI: Are we ready for clinical application? AJR Am J Roentgenol. 2009; 192(6):1550–1557. [PubMed: 19457818]
3. Grenier N, Basseau F, Ries M, Tyndal B, Jones R, Moonen C. Functional MRI of the kidney. Abdom Imaging. 2003; 28(2):164–175. [PubMed: 12592462]
4. Kalb B, Martin DR, Salman K, Sharma P, Votaw J, Larsen C. Kidney transplantation: structural and functional evaluation using MR Nephro-Urography. J Magn Reson Imaging. 2008; 28(4):805–822. [PubMed: 18821623]
5. Nikken JJ, Krestin GP. MRI of the kidney-state of the art. Eur Radiol. 2007; 17(11):2780–2793. [PubMed: 17646992]
6. Li LP, Halter S, Prasad PV. Blood Oxygen Level-Dependent MR Imaging of the Kidneys. Magnetic resonance imaging clinics of North America. 2008; 16(4):613–625. [PubMed: 18926426]
7. Miles KA. Measurement of tissue perfusion by dynamic computed tomography. Br J Radiol. 1991; 64(761):409–412. [PubMed: 2036562]
8. Zhao H, Gong J, Wang Y, Zhang Z, Qin P. Renal hemodynamic changes with aging: a preliminary study using CT perfusion in the healthy elderly. Clin Imaging. 2010; 34(4):247–250. [PubMed: 20630335]
9. Evans RG, Gardiner BS, Smith DW, O’Connor PM. Intrarenal oxygenation: unique challenges and the biophysical basis of homeostasis. American journal of physiology. 2008; 295(5):F1259–1270. [PubMed: 18550645]

10. Brezis M, Rosen S. Hypoxia of the renal medulla--its implications for disease. The New England journal of medicine. 1995; 332(10):647–655. [PubMed: 7845430]

11. Bokacheva L, Rusinek H, Zhang JL, Chen Q, Lee VS. Estimates of glomerular filtration rate from MR renography and tracer kinetic models. J Magn Reson Imaging. 2009; 29(2):371–382. [PubMed: 19161190]

12. Hackstein N, Heckrodt J, Rau WS. Measurement of single-kidney glomerular filtration rate using a contrast-enhanced dynamic gradient-echo sequence and the Rutland-Patlak plot technique. J Magn Reson Imaging. 2003; 18(6):714–725. [PubMed: 14635157]

13. Annet L, Hermoye L, Peeters F, Jamar F, Dehoux JP, Van Beers BE. Glomerular filtration rate: assessment with dynamic contrast-enhanced MRI and a cortical-compartment model in the rabbit kidney. J Magn Reson Imaging. 2004; 20(5):843–849. [PubMed: 15503326]

14. Sourbron SP, Michaely HJ, Reiser MF, Schoenberg SO. MRI-measurement of perfusion and glomerular filtration in the human kidney with a separable compartment model. Investigative radiology. 2008; 43(1):40–48. [PubMed: 18097276]

15. Buckley DL, Shurrab AE, Cheung CM, Jones AP, Mamtora H, Kalra PA. Measurement of single kidney function using dynamic contrast-enhanced MRI: comparison of two models in human subjects. J Magn Reson Imaging. 2006; 24(5):1117–1123. [PubMed: 16941606]

16. Koh TS, Zhang JL, Ong CK, Shuter B. A biphasic parameter estimation method for quantitative analysis of dynamic renal scintigraphic data. Phys Med Biol. 2006; 51(11):2857–2870. [PubMed: 16723771]

17. Rusinek H, Boykov Y, Kaur M, Wong S, Bokacheva L, Sajous JB, Huang AJ, Heller S, Lee VS. Performance of an automated segmentation algorithm for 3D MR renography. Magn Reson Med. 2007; 57(6):1159–1167. [PubMed: 17534915]

18. Zhang JL, Rusinek H, Bokacheva L, Lerman LO, Chen Q, Prince C, Oesingmann N, Song T, Lee VS. Functional assessment of the kidney from magnetic resonance and computed tomography renography: impulse retention approach to a multicompartment model. Magn Reson Med. 2008; 59(2):278–288. [PubMed: 18228576]

19. Lee VS, Rusinek H, Bokacheva L, Huang AJ, Oesingmann N, Chen Q, Kaur M, Prince K, Song T, Kramer EL, Leonard EF. Renal function measurements from MR renography and a simplified multicompartmental model. American journal of physiology. 2007; 292(5):F1548–1559. [PubMed: 17213464]

20. Cutajar M, Mendichovszky IA, Tofts PS, Gordon I. The importance of AIF ROI selection in DCE-MRI renography: reproducibility and variability of renal perfusion and filtration. European journal of radiology. 2010; 74(3):e154–160. [PubMed: 19541441]

21. Mendichovszky IA, Cutajar M, Gordon I. Reproducibility of the aortic input function (AIF) derived from dynamic contrast-enhanced magnetic resonance imaging (DCE-MRI) of the kidneys in a volunteer study. Eur J Radiol. 2009; 71(3):576–581. [PubMed: 19004588]

22. Baumann D, Rudin M. Quantitative assessment of rat kidney function by measuring the clearance of the contrast agent Gd(DOTA) using dynamic MRI. Magn Reson Imaging. 2000; 18(5):587–595. [PubMed: 10913720]

23. Zhang, JL.; Rusinek, H.; Chen, Q.; Storey, P.; Bokacheva, L.; Song, T.; Lee, VS. Assessment of renal function using MR renography without aortic input information. Proceedings of the 16th Annual Meeting of ISMRM; Toronto, Canada. 2008. (abstract 456)

24. Parker GJ, Roberts C, Macdonald A, Buonaccorsi GA, Cheung S, Buckley DL, Jackson A, Watson Y, Davies K, Jayson GC. Experimentally-derived functional form for a population-averaged high-temporal-resolution arterial input function for dynamic contrast-enhanced MRI. Magn Reson Med. 2006; 56(5):993–1000. [PubMed: 17036301]

25. Wang Y, Huang W, Panicek DM, Schwartz LH, Koutcher JA. Feasibility of using limited-population-based arterial input function for pharmacokinetic modeling of osteosarcoma dynamic contrast-enhanced MRI data. Magn Reson Med. 2008; 59(5):1183–1189. [PubMed: 18429032]

26. Roberts C, Buckley DL, Parker GJ. Comparison of errors associated with single- and multi-bolus injection protocols in low-temporal-resolution dynamic contrast-enhanced tracer kinetic analysis. Magn Reson Med. 2006; 56(3):611–619. [PubMed: 16858671]

27. Zhang JL, Rusinek H, Bokacheva L, Chen Q, Storey P, Lee VS. Use of cardiac output to improve measurement of input function in quantitative dynamic contrast-enhanced MRI. J Magn Reson Imaging. 2009; 30(3):656–665. [PubMed: 19711414]
28. Bokacheva L, Rusinek H, Chen Q, Oesingmann N, Prince C, Kaur M, Kramer E, Lee VS. Quantitative determination of Gd-DTPA concentration in T(1)-weighted MR renography studies. Magn Reson Med. 2007; 57(6):1012–1018. [PubMed: 17534906]
29. Shuter B, Tofts PS, Wang SC, Pope JM. The relaxivity of Gd-EOB-DTPA and Gd-DTPA in liver and kidney of the Wistar rat. Magn Reson Imaging. 1996; 14(3):243–253. [PubMed: 8725190]
30. Morkenborg J, Taagehoj JF, Vaever PN, Frokiaer J, Djurhuus JC, Stodkilde-Jorgensen H. In vivo measurement of T1 and T2 relaxivity in the kidney cortex of the pig--based on a two-compartment steady-state model. Magn Reson Imaging. 1998; 16(8):933–942. [PubMed: 9814776]
31. Donahue KM, Weisskoff RM, Burstein D. Water diffusion and exchange as they influence contrast enhancement. J Magn Reson Imaging. 1997; 7(1):102–110. [PubMed: 9039599]
32. Fram EK, Herfkens RJ, Johnson GA, Glover GH, Karis JP, Shimakawa A, Perkins TG, Pelc NJ. Rapid calculation of T1 using variable flip angle gradient refocused imaging. Magn Reson Imaging. 1987; 5(3):201–208. [PubMed: 3626789]
33. Scheffler K, Hennig J. T(1) quantification with inversion recovery TrueFISP. Magn Reson Med. 2001; 45(4):720–723. [PubMed: 11284003]
34. Bokacheva L, Huang AJ, Chen Q, Oesingmann N, Storey P, Rusinek H, Lee VS. Single breath-hold T1 measurement using low flip angle TrueFISP. Magn Reson Med. 2006; 55(5):1186–1190. [PubMed: 16572392]
35. de Senneville BD, Mendichovszky IA, Roujol S, Gordon I, Moonen C, Grenier N. Improvement of MRI-functional measurement with automatic movement correction in native and transplanted kidneys. J Magn Reson Imaging. 2008; 28(4):970–978. [PubMed: 18846555]
36. Giele EL, de Priester JA, Blom JA, den Boer JA, van Engelshoven JM, Hasman A, Geerlings M. Movement correction of the kidney in dynamic MRI scans using FFT phase difference movement detection. J Magn Reson Imaging. 2001; 14(6):741–749. [PubMed: 11747031]
37. Li S, Zollner FG, Merrem AD, Peng Y, Roervik J, Lundervold A, Schad LR. Wavelet-based segmentation of renal compartments in DCE-MRI of human kidney: Initial results in patients and healthy volunteers. Comput Med Imaging Graph. 2011
38. Liu, J.; Leong, TY.; Chee, KB.; Tan, BP.; Shuter, B.; Wang, SC. Set-based Cascading Approaches for Magnetic Resonance (MR) Image Segmentation (SCAMIS). AMIA Annual Symposium proceedings / AMIA Symposium AMIA Symposium; 2006. p. 504-508.
39. Gutierrez DR, Wells K, Montesdeoca O Diaz, Santana A Moran, Mendichovszky IA, Gordon I. Partial volume effects in dynamic contrast magnetic resonance renal studies. European journal of radiology. 2010; 75(2):221–229. [PubMed: 19501996]
40. Grobner T. Gadolinium--a specific trigger for the development of nephrogenic fibrosing dermopathy and nephrogenic systemic fibrosis? Nephrol Dial Transplant. 2006; 21(4):1104–1108. [PubMed: 16431890]
41. Marckmann P, Skov L, Rossen K, Dupont A, Damholt MB, Heaf JG, Thomsen HS. Nephrogenic systemic fibrosis: suspected causative role of gadodiamide used for contrast-enhanced magnetic resonance imaging. J Am Soc Nephrol. 2006; 17(9):2359–2362. [PubMed: 16885403]
42. Taylor A, Nally J, Aurell M, Blaufox D, Dondi M, Dubovsky E, Fine E, Fommei E, Geyskes G, Granerus G, Kahn D, Morton K, Oei HY, Russell C, Sfakianakis G, Fletcher J. Consensus report on ACE inhibitor renography for detecting renovascular hypertension. Radionuclides in Nephrourology Group. Consensus Group on ACEI Renography. J Nucl Med. 1996; 37(11):1876–1882. [PubMed: 8917196]
43. Grenier N, Trillaud H, Combe C, Degreze P, Jeandot R, Gosse P, Douws C, Palussiere J. Diagnosis of renovascular hypertension: feasibility of captopril-sensitized dynamic MR imaging and comparison with captopril scintigraphy. AJR Am J Roentgenol. 1996; 166(4):835–843. [PubMed: 8610560]
44. Zhang JL, Rusinek H, Bokacheva L, Lim RP, Chen Q, Storey P, Prince K, Hecht EM, Kim DC, Lee VS. Angiotensin-converting enzyme inhibitor-enhanced MR renography: repeated measures

of GFR and RPF in hypertensive patients. American journal of physiology. 2009; 296(4):F884–891. [PubMed: 19158343]

45. Lee VS, Rusinek H, Johnson G, Rofsky NM, Krinsky GA, Weinreb JC. MR renography with low-dose gadopentetate dimeglumine: feasibility. Radiology. 2001; 221(2):371–379. [PubMed: 11687678]
46. Grattan-Smith JD, Perez-Bayfield MR, Jones RA, Little S, Broecker B, Smith EA, Scherz HC, Kirsch AJ. MR imaging of kidneys: functional evaluation using F-15 perfusion imaging. Pediatr Radiol. 2003; 33(5):293–304. [PubMed: 12695861]
47. McDaniel BB, Jones RA, Scherz H, Kirsch AJ, Little SB, Grattan-Smith JD. Dynamic contrast-enhanced MR urography in the evaluation of pediatric hydronephrosis: Part 2, anatomic and functional assessment of uteropelvic junction obstruction. AJR Am J Roentgenol. 2005; 185(6):1608–1614. [PubMed: 16304022]
48. Rohrschneider WK, Haufe S, Wiesel M, Tonshoff B, Wunsch R, Darge K, Clorius JH, Troger J. Functional and morphologic evaluation of congenital urinary tract dilatation by using combined static-dynamic MR urography: findings in kidneys with a single collecting system. Radiology. 2002; 224(3):683–694. [PubMed: 12202700]
49. Grattan-Smith JD, Little SB, Jones RA. MR urography evaluation of obstructive uropathy. Pediatr Radiol. 2008; 38(Suppl 1):S49–69. [PubMed: 18071689]
50. Jones RA, Perez-Brayfield MR, Kirsch AJ, Grattan-Smith JD. Renal transit time with MR urography in children. Radiology. 2004; 233(1):41–50. [PubMed: 15317951]
51. Szolar DH, Preidler K, Ebner F, Kammerhuber F, Horn S, Ratschek M, Ranner G, Petritsch P, Horina JH. Functional magnetic resonance imaging of human renal allografts during the post-transplant period: preliminary observations. Magn Reson Imaging. 1997; 15(7):727–735. [PubMed: 9309603]
52. Agildere AM, Tarhan NC, Bozdagi G, Demirag A, Niron EA, Haberal M. Correlation of quantitative dynamic magnetic resonance imaging findings with pathology results in renal transplants: a preliminary report. Transplant Proc. 1999; 31(8):3312–3316. [PubMed: 10616489]
53. Wentland AL, Sadowski EA, Djamali A, Grist TM, Becker BN, Fain SB. Quantitative MR measures of intrarenal perfusion in the assessment of transplanted kidneys: initial experience. Acad Radiol. 2009; 16(9):1077–1085. [PubMed: 19539502]
54. Yamamoto, A.; Zhang, JL.; Rusinek, H.; Chandarana, H.; Babb, JS.; Diflo, T.; John, D.; Benstein, J.; Vivier, PH.; Stoffel, D.; VS., L. Quantitative evaluation of acute renal transplant dysfunction with low-dose 3D MR renography. Proceedings of the 18th Annual Meeting of ISMRM; Stockholm, Sweden. 2010. (abstract 4691)
55. Kim S, Naik M, Sigmund E, Taouli B. Diffusion-weighted MR imaging of the kidneys and the urinary tract. Magn Reson Imaging Clin N Am. 2008; 16(4):585–596. vii–viii. [PubMed: 18926424]
56. Namimoto T, Yamashita Y, Mitsuzaki K, Nakayama Y, Tang Y, Takahashi M. Measurement of the apparent diffusion coefficient in diffuse renal disease by diffusion-weighted echo-planar MR imaging. J Magn Reson Imaging. 1999; 9(6):832–837. [PubMed: 10373031]
57. Thoeny HC, De Keyzer F, Oyen RH, Peeters RR. Diffusion-weighted MR imaging of kidneys in healthy volunteers and patients with parenchymal diseases: initial experience. Radiology. 2005; 235(3):911–917. [PubMed: 15845792]
58. Toyoshima S, Noguchi K, Seto H, Shimizu M, Watanabe N. Functional evaluation of hydronephrosis by diffusion-weighted MR imaging. Relationship between apparent diffusion coefficient and split glomerular filtration rate. Acta Radiol. 2000; 41(6):642–646. [PubMed: 11092490]
59. Carbone SF, Gaggioli E, Ricci V, Mazzei F, Mazzei MA, Volterrani L. Diffusion-weighted magnetic resonance imaging in the evaluation of renal function: a preliminary study. La Radiologia medica. 2007; 112(8):1201–1210. [PubMed: 18074195]
60. Togao O, Doi S, Kuro-o M, Masaki T, Yorioka N, Takahashi M. Assessment of renal fibrosis with diffusion-weighted MR imaging: study with murine model of unilateral ureteral obstruction. Radiology. 2010; 255(3):772–780. [PubMed: 20406881]

61. Thoeny HC, Grenier N. Science to practice: Can diffusion-weighted MR imaging findings be used as biomarkers to monitor the progression of renal fibrosis? Radiology. 2010; 255(3):667–668. [PubMed: 20501704]
62. Le Bihan D, Breton E, Lallemand D, Aubin ML, Vignaud J, Laval-Jeantet M. Separation of diffusion and perfusion in intravoxel incoherent motion MR imaging. Radiology. 1988; 168(2): 497–505. [PubMed: 3393671]
63. Le Bihan D, Turner R. The capillary network: a link between IVIM and classical perfusion. Magn Reson Med. 1992; 27(1):171–178. [PubMed: 1435202]
64. Zhang JL, Sigmund EE, Chandarana H, Rusinek H, Chen Q, Vivier PH, Taouli B, Lee VS. Variability of renal apparent diffusion coefficients: limitations of the monoexponential model for diffusion quantification. Radiology. 2010; 254(3):783–792. [PubMed: 20089719]
65. Wittsack HJ, Lanzman RS, Mathys C, Janssen H, Modder U, Blondin D. Statistical evaluation of diffusion-weighted imaging of the human kidney. Magn Reson Med. 2010; 64(2):616–622. [PubMed: 20665805]
66. Zhang JL, Sigmund EE, Rusinek H, Chandarana H, Storey P, Chen Q, Lee VS. Optimization of b-value sampling for diffusion-weighted imaging of the kidney. Magn Reson Med. 2011
67. Ogawa S, Lee TM, Kay AR, Tank DW. Brain magnetic resonance imaging with contrast dependent on blood oxygenation. Proceedings of the National Academy of Sciences of the United States of America. 1990; 87(24):9868–9872. [PubMed: 2124706]
68. Tumkur S, Vu A, Li L, Prasad PV. Evaluation of intrarenal oxygenation at 3.0 T using 3-dimensional multiple gradient-recalled echo sequence. Investigative radiology. 2006; 41(2):181–184. [PubMed: 16428990]
69. Prasad PV, Edelman RR, Epstein FH. Noninvasive evaluation of intrarenal oxygenation with BOLD MRI. Circulation. 1996; 94(12):3271–3275. [PubMed: 8989140]
70. Tumkur SM, Vu AT, Li LP, Pierchala L, Prasad PV. Evaluation of intra-renal oxygenation during water diuresis: a time-resolved study using BOLD MRI. Kidney international. 2006; 70(1):139–143. [PubMed: 16572109]
71. Li LP, Storey P, Pierchala L, Li W, Polzin J, Prasad P. Evaluation of the reproducibility of intrarenal R2* and DeltaR2* measurements following administration of furosemide and during waterload. J Magn Reson Imaging. 2004; 19(5):610–616. [PubMed: 15112311]
72. Simon-Zoula SC, Hofmann L, Giger A, Vogt B, Vock P, Frey FJ, Boesch C. Noninvasive monitoring of renal oxygenation using BOLD-MRI: a reproducibility study. NMR in biomedicine. 2006; 19(1):84–89. [PubMed: 16411163]
73. Thoeny HC, Zumstein D, Simon-Zoula S, Eisenberger U, De Keyzer F, Hofmann L, Vock P, Boesch C, Frey FJ, Vermathen P. Functional evaluation of transplanted kidneys with diffusion-weighted and BOLD MR imaging: initial experience. Radiology. 2006; 241(3):812–821. [PubMed: 17114628]
74. Juillard L, Lerman LO, Kruger DG, Haas JA, Rucker BC, Polzin JA, Riederer SJ, Romero JC. Blood oxygen level-dependent measurement of acute intra-renal ischemia. Kidney international. 2004; 65(3):944–950. [PubMed: 14871414]
75. Textor SC, Glockner JF, Lerman LO, Misra S, McKusick MA, Riederer SJ, Grande JP, Gomez SI, Romero JC. The use of magnetic resonance to evaluate tissue oxygenation in renal artery stenosis. J Am Soc Nephrol. 2008; 19(4):780–788. [PubMed: 18287564]
76. Sadowski EA, Fain SB, Alford SK, Korosec FR, Fine J, Muehrer R, Djamali A, Hofmann RM, Becker BN, Grist TM. Assessment of acute renal transplant rejection with blood oxygen level-dependent MR imaging: initial experience. Radiology. 2005; 236(3):911–919. [PubMed: 16118170]
77. Djamali A, Sadowski EA, Samaniego-Picota M, Fain SB, Muehrer RJ, Alford SK, Grist TM, Becker BN. Noninvasive assessment of early kidney allograft dysfunction by blood oxygen level-dependent magnetic resonance imaging. Transplantation. 2006; 82(5):621–628. [PubMed: 16969284]
78. Han F, Xiao W, Xu Y, Wu J, Wang Q, Wang H, Zhang M, Chen J. The significance of BOLD MRI in differentiation between renal transplant rejection and acute tubular necrosis. Nephrol Dial Transplant. 2008; 23(8):2666–2672. [PubMed: 18308769]

79. Hasslacher, C.; Böhm, S. Diabetes and the kidney : diabetic nephropathy : prevention, diagnosis, treatment. Wiley; Chichester, West Sussex, England: 2004. p. xiiip. 132

80. Epstein FH, Veves A, Prasad PV. Effect of diabetes on renal medullary oxygenation during water diuresis. Diabetes care. 2002; 25(3):575–578. [PubMed: 11874950]

81. dos Santos EA, Li LP, Ji L, Prasad PV. Early changes with diabetes in renal medullary hemodynamics as evaluated by fiberoptic probes and BOLD magnetic resonance imaging. Investigative radiology. 2007; 42(3):157–162. [PubMed: 17287645]

82. Ries M, Basseau F, Tyndal B, Jones R, Deminiere C, Catargi B, Combe C, Moonen CW, Grenier N. Renal diffusion and BOLD MRI in experimental diabetic nephropathy. Blood oxygen level-dependent. J Magn Reson Imaging. 2003; 17(1):104–113. [PubMed: 12500279]

83. Pedersen M, Dissing TH, Morkenborg J, Stodkilde-Jorgensen H, Hansen LH, Pedersen LB, Grenier N, Frokiaer J. Validation of quantitative BOLD MRI measurements in kidney: application to unilateral ureteral obstruction. Kidney international. 2005; 67(6):2305–2312. [PubMed: 15882272]

84. Thoeny HC, Kessler TM, Simon-Zoula S, De Keyzer F, Mohaupt M, Studer UE, Vermathen P. Renal oxygenation changes during acute unilateral ureteral obstruction: assessment with blood oxygen level-dependent mr imaging--initial experience. Radiology. 2008; 247(3):754–761. [PubMed: 18403623]

85. Xiao WB, Wang QD, Xu JJ, Han F, Zhang MM. Evaluation of kidney oxygen bioavailability in acute renal failure by blood oxygen level dependent magnetic resonance imaging. Zhejiang Da Xue Xue Bao Yi Xue Ban. 2010; 39(2):157–162. [PubMed: 20387243]

86. Detre JA, Zhang W, Roberts DA, Silva AC, Williams DS, Grandis DJ, Koretsky AP, Leigh JS. Tissue specific perfusion imaging using arterial spin labeling. NMR Biomed. 1994; 7(1-2):75–82. [PubMed: 8068529]

87. Buxton RB, Frank LR, Wong EC, Siewert B, Warach S, Edelman RR. A general kinetic model for quantitative perfusion imaging with arterial spin labeling. Magn Reson Med. 1998; 40(3):383–396. [PubMed: 9727941]

88. Song R, Loeffler RB, Hillenbrand CM. Improved renal perfusion measurement with a dual navigator-gated Q2TIPS fair technique. Magn Reson Med. 2010; 64(5):1352–1359. [PubMed: 20593428]

89. Kiefer C, Schroth G, Gralla J, Diehm N, Baumgartner I, Husmann M. A feasibility study on model-based evaluation of kidney perfusion measured by means of FAIR prepared true-FISP arterial spin labeling (ASL) on a 3-T MR scanner. Academic radiology. 2009; 16(1):79–87. [PubMed: 19064215]

90. Artz NS, Sadowski EA, Wentland AL, Grist TM, Seo S, Djamali A, Fain SB. Arterial spin labeling MRI for assessment of perfusion in native and transplanted kidneys. Magn Reson Imaging. 2011; 29(1):74–82. [PubMed: 20850241]

91. Notohamiprodjo M, Dietrich O, Horger W, Horng A, Helck AD, Herrmann KA, Reiser MF, Glaser C. Diffusion tensor imaging (DTI) of the kidney at 3 tesla-feasibility, protocol evaluation and comparison to 1.5 Tesla. Invest Radiol. 2010; 45(5):245–254. [PubMed: 20375845]

92. Cheung JS, Fan SJ, Chow AM, Zhang J, Man K, Wu EX. Diffusion tensor imaging of renal ischemia reperfusion injury in an experimental model. NMR Biomed. 2010; 23(5):496–502. [PubMed: 20175152]

93. Chandarana, H.; Hecht, EM.; Taouli, B.; E., S. Diffusion tensor imaging of in vivo human kidney at 3 T: robust anisotropy measurement in the medulla. Proceedings of the 16th Annual Meeting of ISMRM; Toronto, Canada. 2008. (abstract 494)

94. Maril N, Rosen Y, Reynolds GH, Ivanishev A, Ngo L, Lenkinski RE. Sodium MRI of the human kidney at 3 Tesla. Magn Reson Med. 2006; 56(6):1229–1234. [PubMed: 17089361]

95. Rosen Y, Lenkinski RE. Sodium MRI of a human transplanted kidney. Academic radiology. 2009; 16(7):886–889. [PubMed: 19375951]

96. Atthe BK, Babsky AM, Hopewell PN, Phillips CL, Molitoris BA, Bansal N. Early monitoring of acute tubular necrosis in the rat kidney by 23Na-MRI. American journal of physiology. 2009; 297(5):F1288–1298. [PubMed: 19726545]

97. Warner L, Yin M, Glaser KJ, Woollard JA, Carrascal CA, Korsmo MJ, Crane JA, Ehman RL, Lerman LO. Noninvasive in vivo assessment of renal tissue elasticity during graded renal ischemia using MR elastography. Investigative radiology. 2011 Epub ahead of print. DOI: 10.1097/RLI.0b013e3182183a95.

98. Shah NS, Kruse SA, Lager DJ, Farell-Baril G, Lieske JC, King BF, Ehman RL. Evaluation of renal parenchymal disease in a rat model with magnetic resonance elastography. Magn Reson Med. 2004; 52(1):56–64. [PubMed: 15236367]

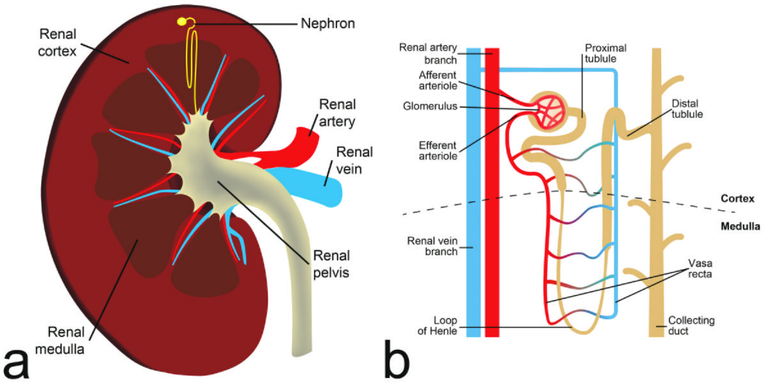

Figure 1.

(a) Coronal section of the kidney; (b) schematic diagram of a nephron.

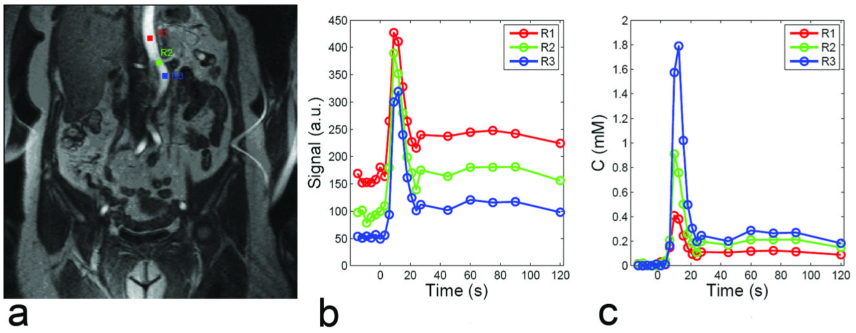

Figure 2.

Variability of AIF in DCE MRI. Regions of interest at different levels of aorta (a) suffer from different degrees of inflow artifact (b), resulting in AIFs of different magnitudes (c).

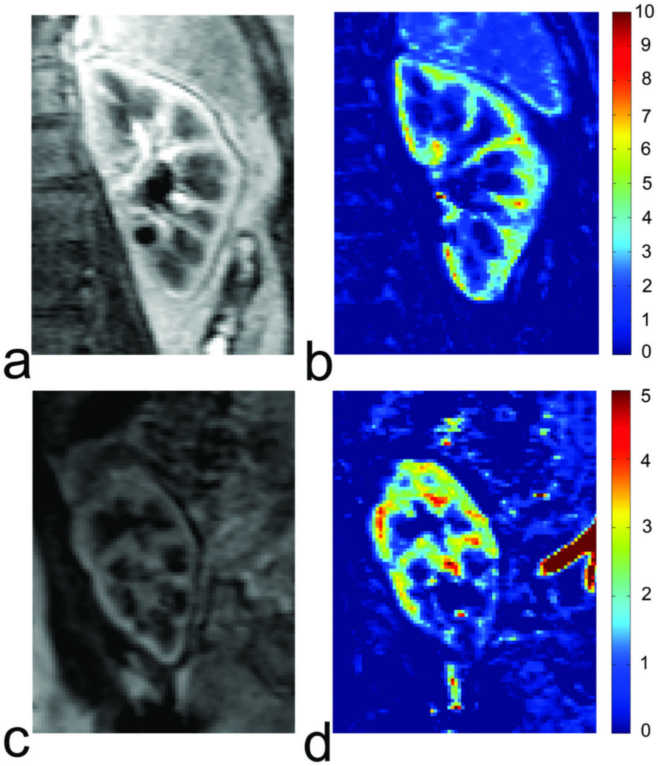

Figure 3.

Comparison of DCE MRI for a healthy kidney and a partially ischemic transplant. (a) One image of the healthy kidney from post-contrast vascular phase; (b) the perfusion map of the healthy kidney generated from vascular-phase images; (c) one image of the renal transplant from post-contrast vascular phase; (d) the perfusion map of the transplant showing partial ischemia.

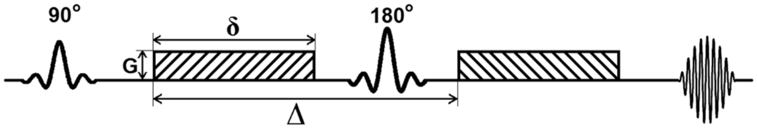

Figure 4.

Diagram of typical DWI sequence. δ is the duration of diffusion-encoding gradient lobe, Δ is the time between the gradient lobes, G is the magnitude of the gradient.

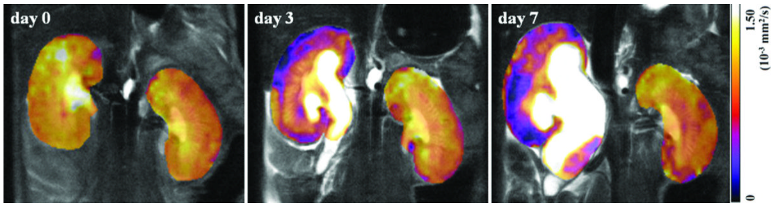

Figure 5.

Coronal ADC maps of the kidneys in a mouse before UUO (day 0) and on days 3 and 7 after UUO. Reprinted with permission from RSNA (60).

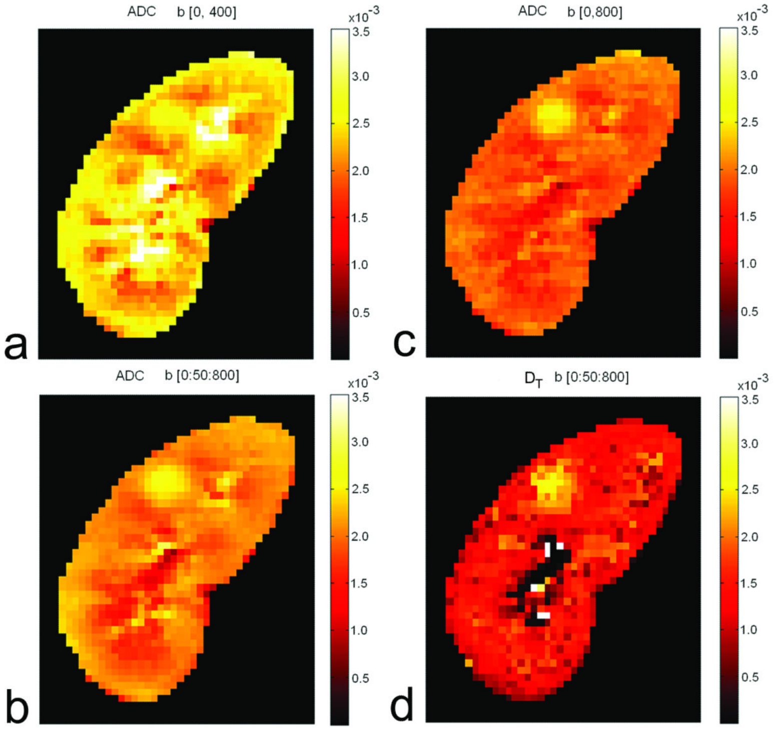

Figure 6.

ADC value from mono-exponential analysis depends heavily on the b values used: (a) ADC map from b values 0 and 400 s/mm^2; (b) ADC map from b values 0 and 800 s/mm^2; (c) ADC map from all b values from 0 to 800 with interval of 50 s/mm^2. For comparison, D_T map from bi-exponential analysis is shown in (d).

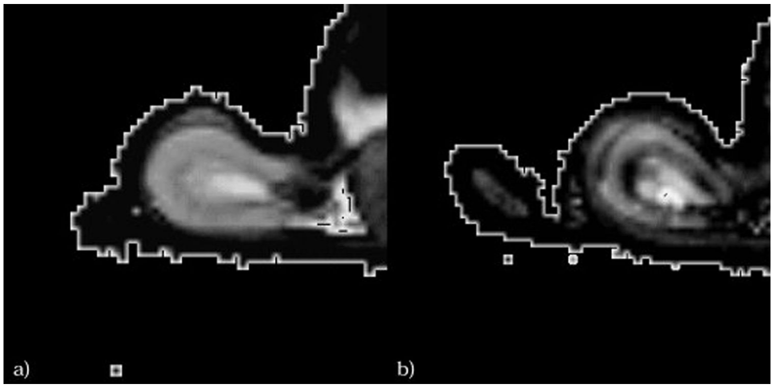

Figure 7.

T_2* maps of (a) healthy and (b) diabetic kidneys for comparison. In both cases, the lowest T_2* values clearly are found within the outer stripe of the outer medulla. Note that low T_2* value corresponds to low oxygenation. Reprinted with permission from John Willy and Sons (82).

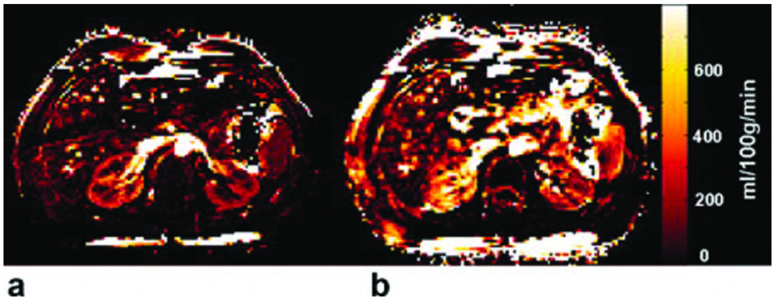

Figure 8.

Axial perfusion rate maps obtained by FAIR True-FISP with (a) and without (b) the dual navigator-gated technique in the same scale. The kidneys are clearly delineated in the dual navigator-gated FAIR True-FISP perfusion image (a). The perfusion values in (b) (without navigator gating) are overestimated because of respiratory motion. Reprinted with permission from John Willy and Sons (88).

Table 1

MRI tools for renal functional assessment

Physiologic parameters	**MRI tools**
Perfusion	ASL, DCE, DWI(IVIM)
Glomerular filtration	DCE
Interstitial diffusion	DWI
Tissue oxygenation	BOLD
Tubular transit, Sodium concentration	Largely unexplored